Supporting Information

Exploring heterostructures of d-block metal oxides coupled to ZnO for the Electrochemical Reduction of CO₂

Ilias Stamatelos^{a,b}, Gelson T. S. T. da Silva^c, Caue Ribeiro^{d*}, Meital Shviro^e

^a Forschungszentrum Jülich GmbH, Institute of Energy and Climate Research: Electrochemical Process Engineering (IEK-14), 52425 Jülich, Germany.

^b Faculty of Mechanical Engineering, RWTH Aachen University, 52056 Aachen, Germany

^c Interdisciplinary Laboratory of Electrochemistry and Ceramics, Department of Chemistry, Federal University of Sao Carlos, São Carlos, SP, 13565905, Brazil.

^d Nanotechnology National Laboratory for Agriculture (LNNA), Embrapa Instrumentation, São Carlos, SP, 13561206, Brazil.

^e Chemistry and Nanoscience Center, National Renewable Energy Laboratory (NREL), Golden, CO, 80401, United States

 \Box To whom correspondence should be addressed;

caue.ribeiro@embrapa.br

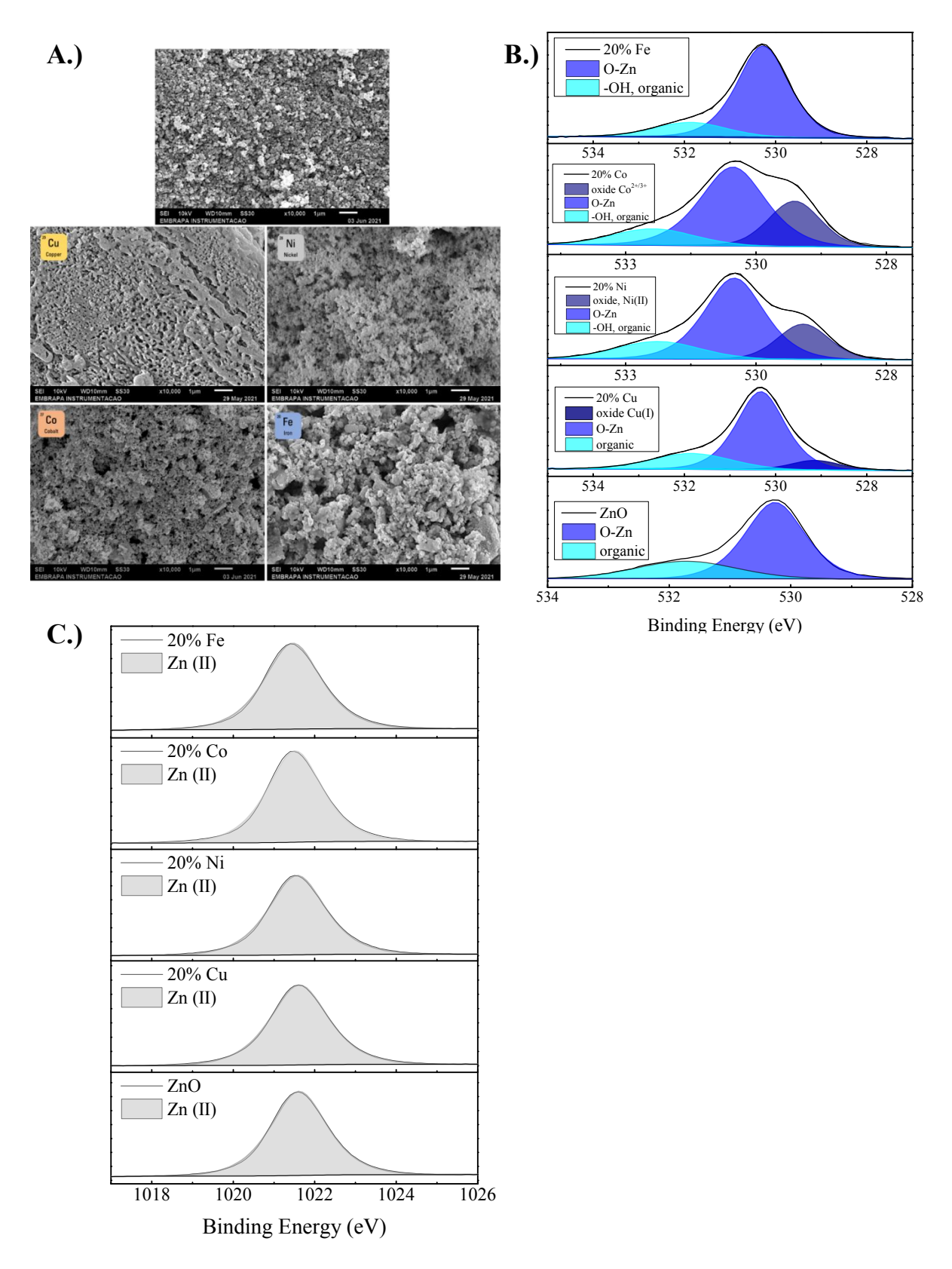


Figure S1: Physical characterizations of the d-block metals heterostructured ZnO-based catalyst materials, A.) SEM images of the different powders, B.) High-resolution oxygen-XPS of the pristine catalyst powders, C.) High-resolution Zn-2p3 XPS of the pristine catalyst powders.

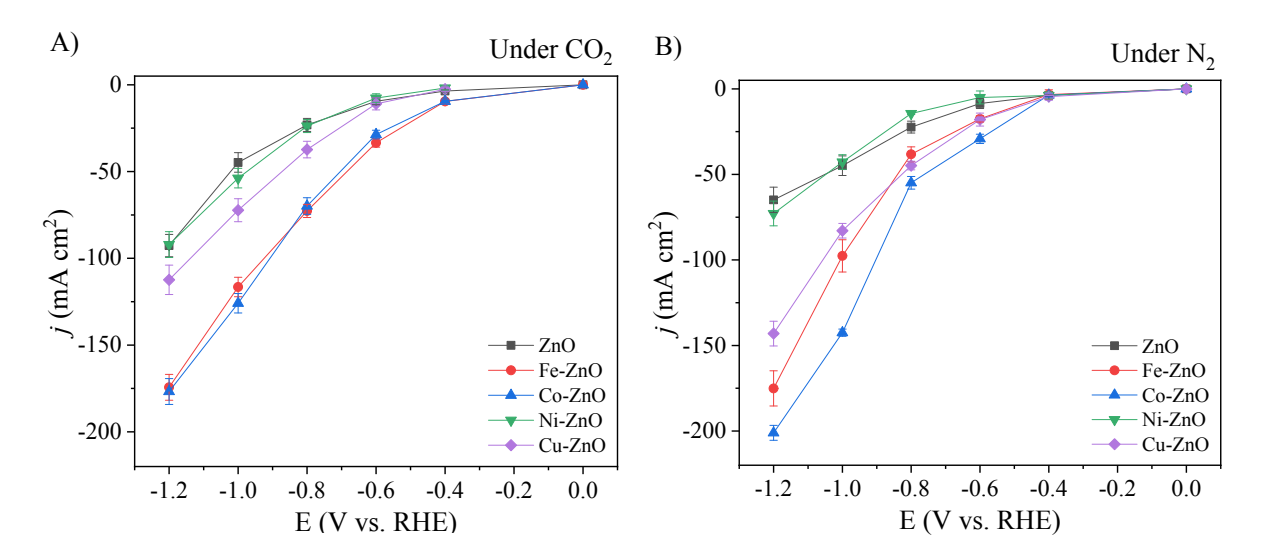


Figure S2: Polarization curves of the catalyst-loaded GDEs. The measurements were conducted in the flow cell at alkaline conditions (1 M KOH). A.) Performance at CO₂ feed 20 sccm (ECR favoring environment), B.) Performance at N₂ feed 20 sccm (HER favoring environment).

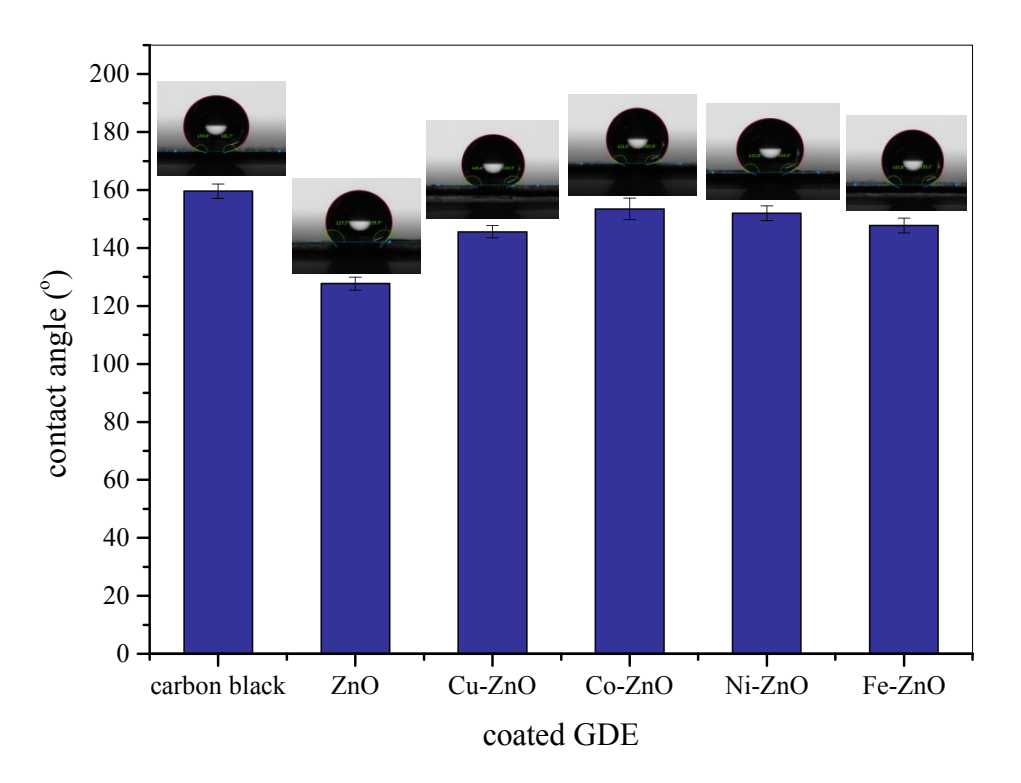


Figure S3: Contact angle of catalyst-coated GDEs. Using a DI water droplet, they were measured under static conditions at room temperature.

The contact angle of the 'reveals similar hydrophobic environments for all the different catalyst materials. The catalyst-loaded GDEs present a lower contact angle than the blank sample (GDE coated with carbon black ink). The latest is related to ZnO's stronger affinity and the d-block metals with the $\rm H_2O$.

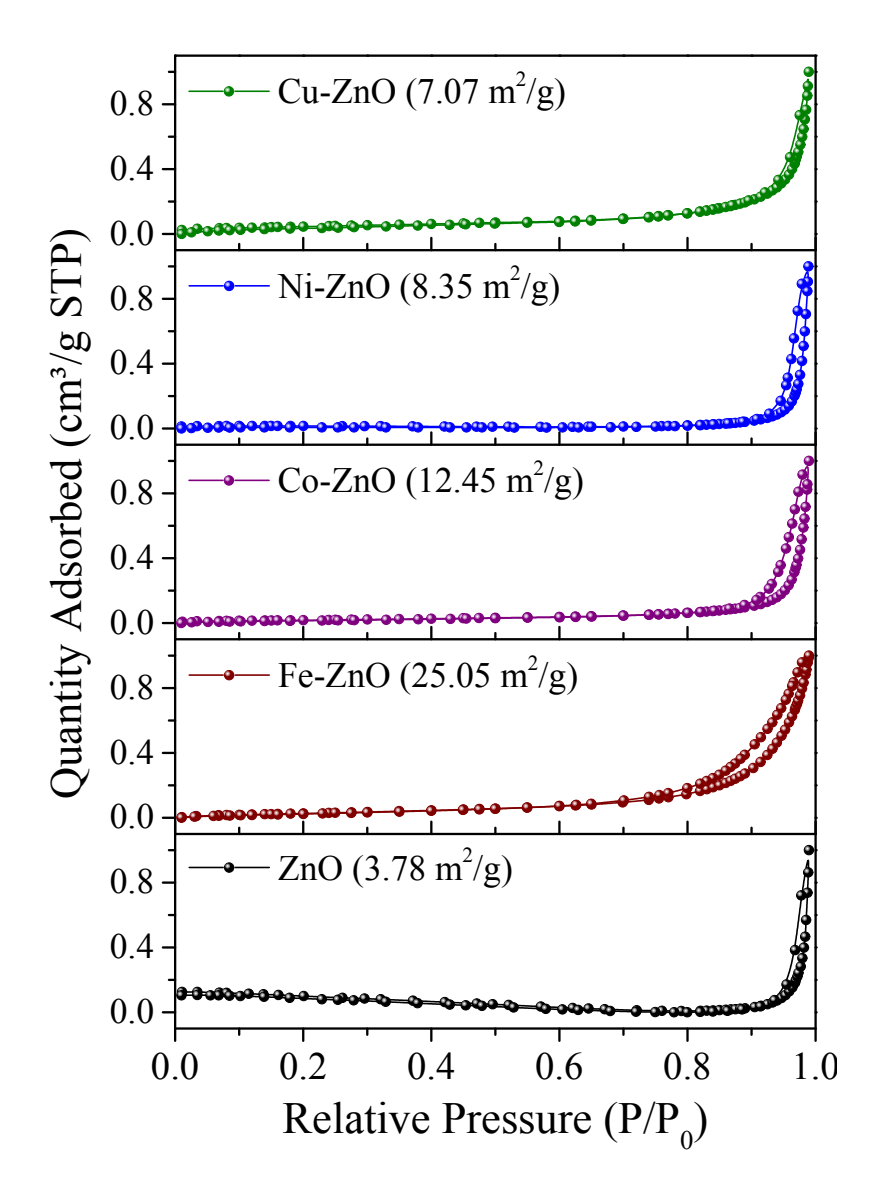


Figure S4: N₂ physisorption isotherms and specific surface area (SSAs) of the prepared materials.

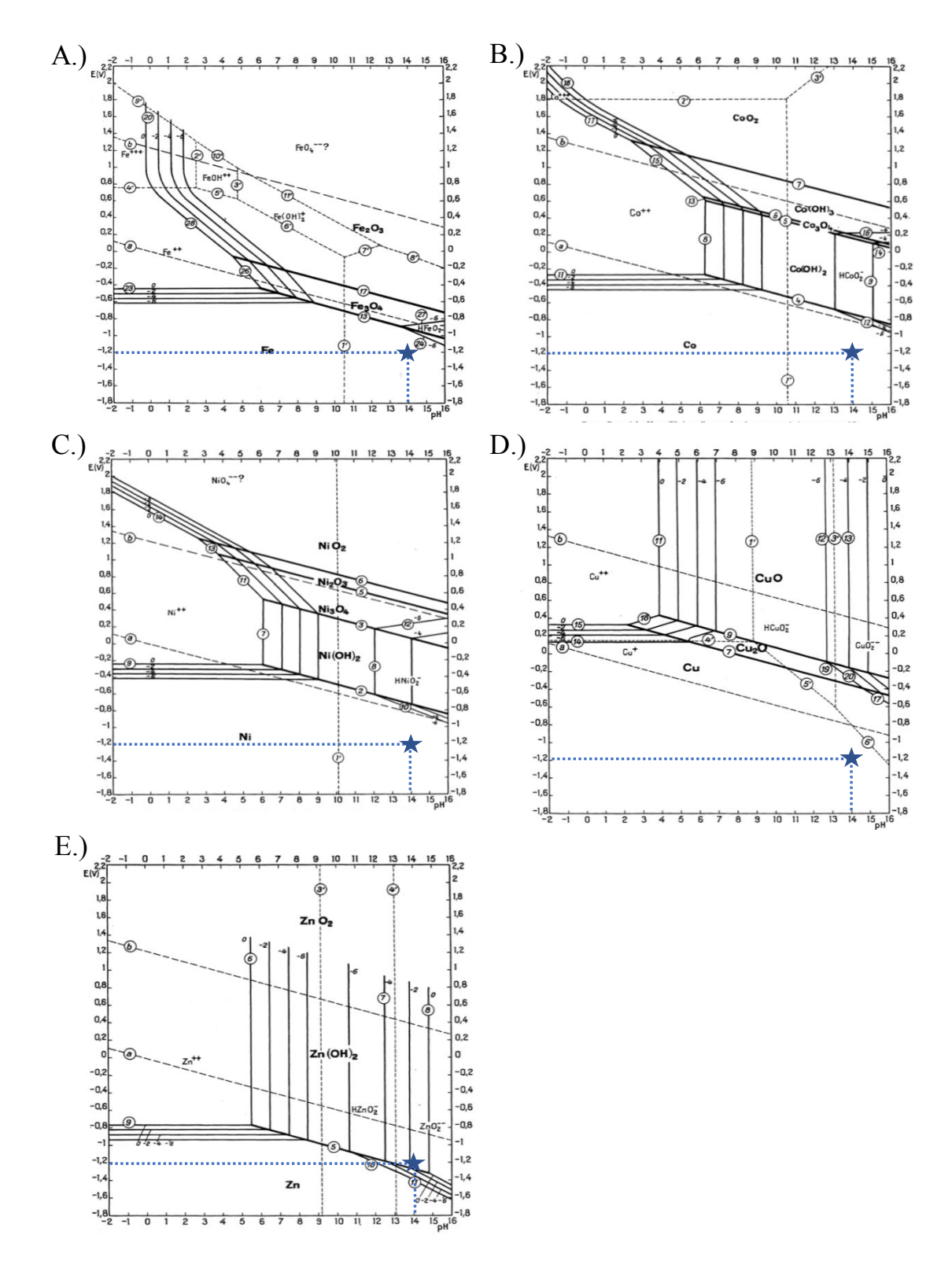


Figure S5: Pourbaix diagrams of the catalyst materials at room temperature A.) Fe-ZnO, B.) Co-ZnO, C.) Ni-ZnO, D.) Cu-ZnO, E.) ZnO.

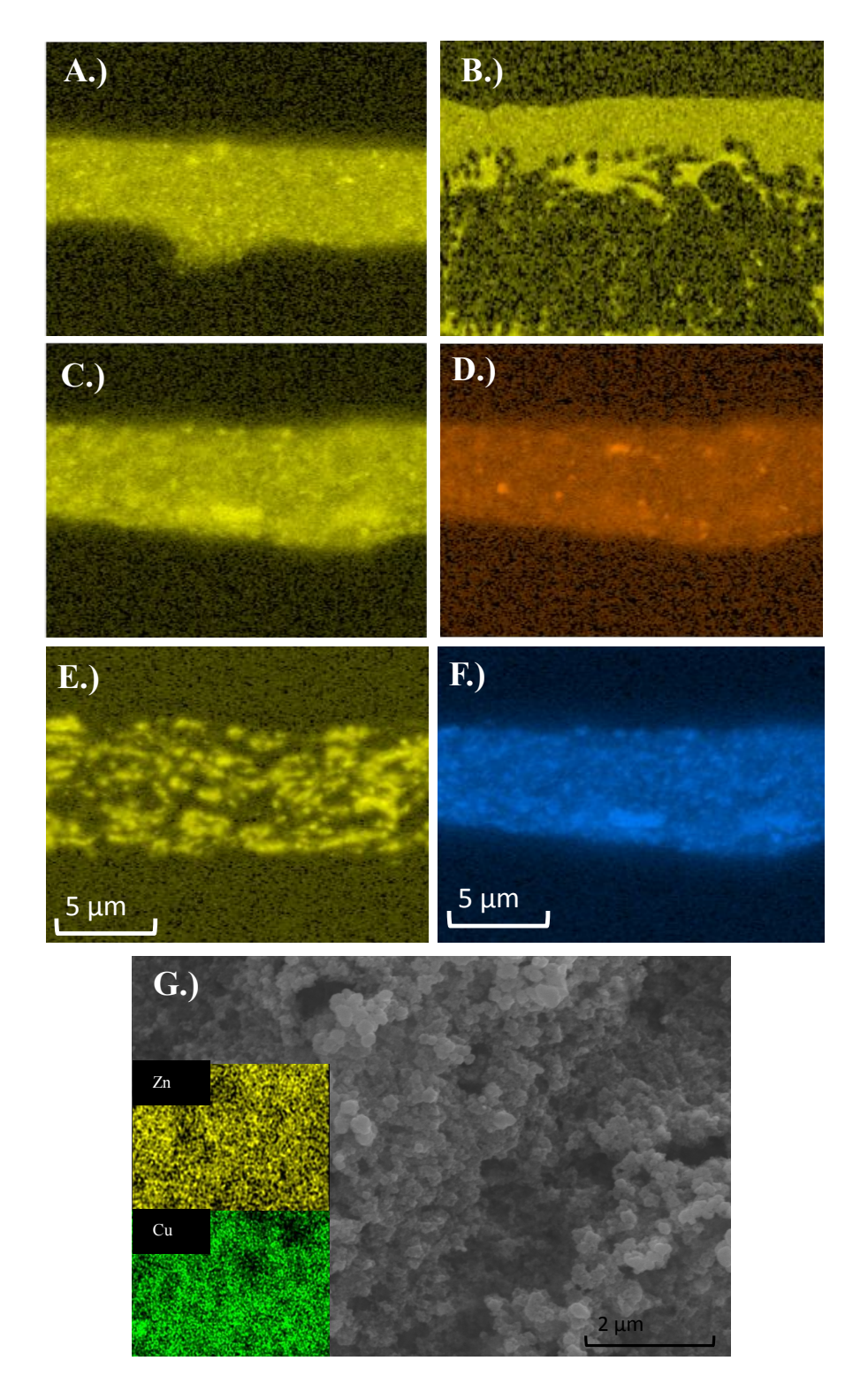


Figure S6: SEM-EDX images of the ZnO and Cu-ZnO GDEs cross-sections before and after long-term ECR. A.) Zn mapping of the pristine ZnO GDE, B.) Zn mapping of the ZnO GDE after the test, C.) Zn mapping of the pristine Cu-ZnO GDE, D.) Cu mapping of the pristine Cu-ZnO GDE, E.) Zn mapping of the Cu-ZnO GDE after the test, F.) Cu mapping of the Cu-ZnO GDE after the test, G.) SEM and EDX of the catalyst layer of the as-prepared Cu-ZnO GDE.

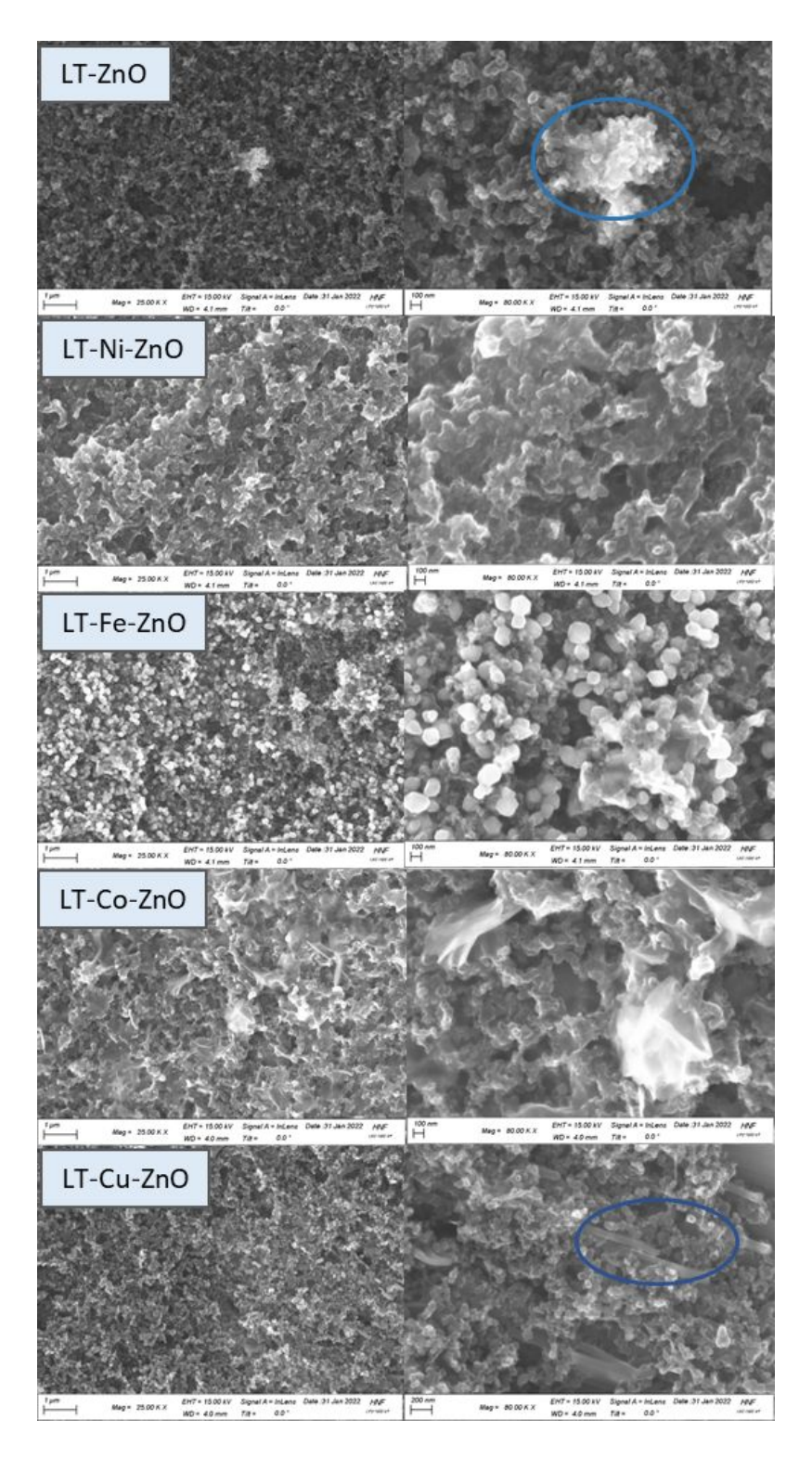


Figure S7: The SEM images of the catalyst-loaded GDEs after the long-term (LT) testing at $1.4~V_{RHE}$. The experiments were conducted under our usual ECR conditions in Flow-Cell configuration at alkaline pH (1 M KOH).

The SEM images captured after the extended operation reveal intricate insights into the degradation of the catalyst layer. Notably highlighted by the blue lines are the aggregates and precipitates that have developed within the catalyst layer of the GDE. The ZnO-GDEs exhibit aggregates of the ZnO material that undermine its active surface. The diffused and extended agglomeration of the catalyst material is more evident in the case of the Ni-, Fe- and Co-doped ZnO-GDEs. The uneven and degraded morphology of the final surface shows that the performance of the GDE has degraded. Finally, rod-like structures can be seen penetrating the surface of the Cu-ZnO GDE. It is attributed to the formation of potassium carbonate precipitates on the catalyst layer. The impaired hydrophobicity of the surface is responsible for the extensive formation and deep penetration of the precipitates.

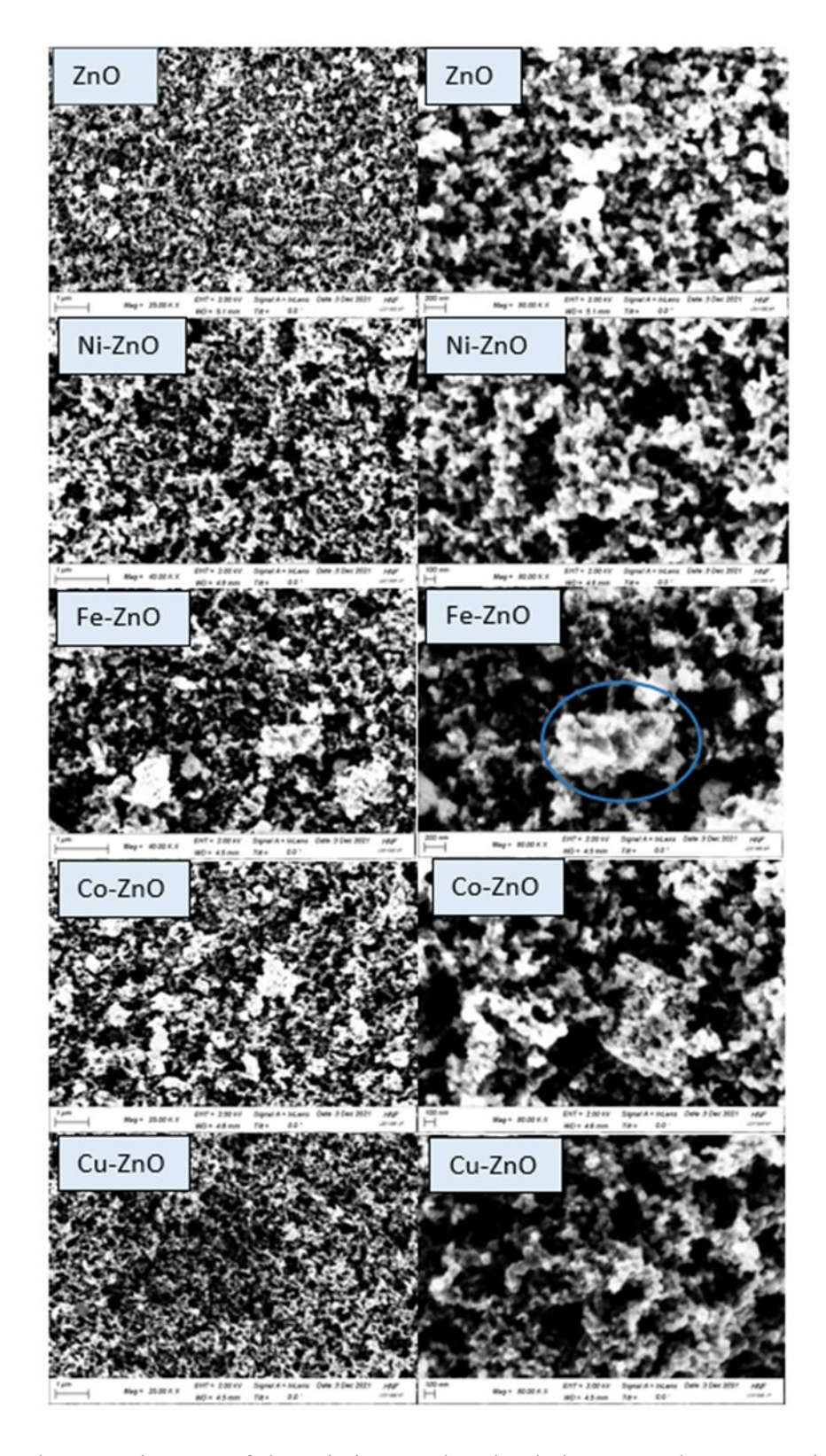


Figure S8: The SEM images of the pristine catalyst-loaded GDEs. The contrast indicates the uniform distribution among the oxide-based and the carbon-black particles.

The SEM images of the initial GDEs (Figure S8) show a uniform catalyst layer. Only in the case of Fe-ZnO GDEs the formation of Fe-ZnO agglomerates is observed. The higher magnification shows a good distribution of the ZnO-based nanoparticles for all of the catalyst-loaded GDEs.

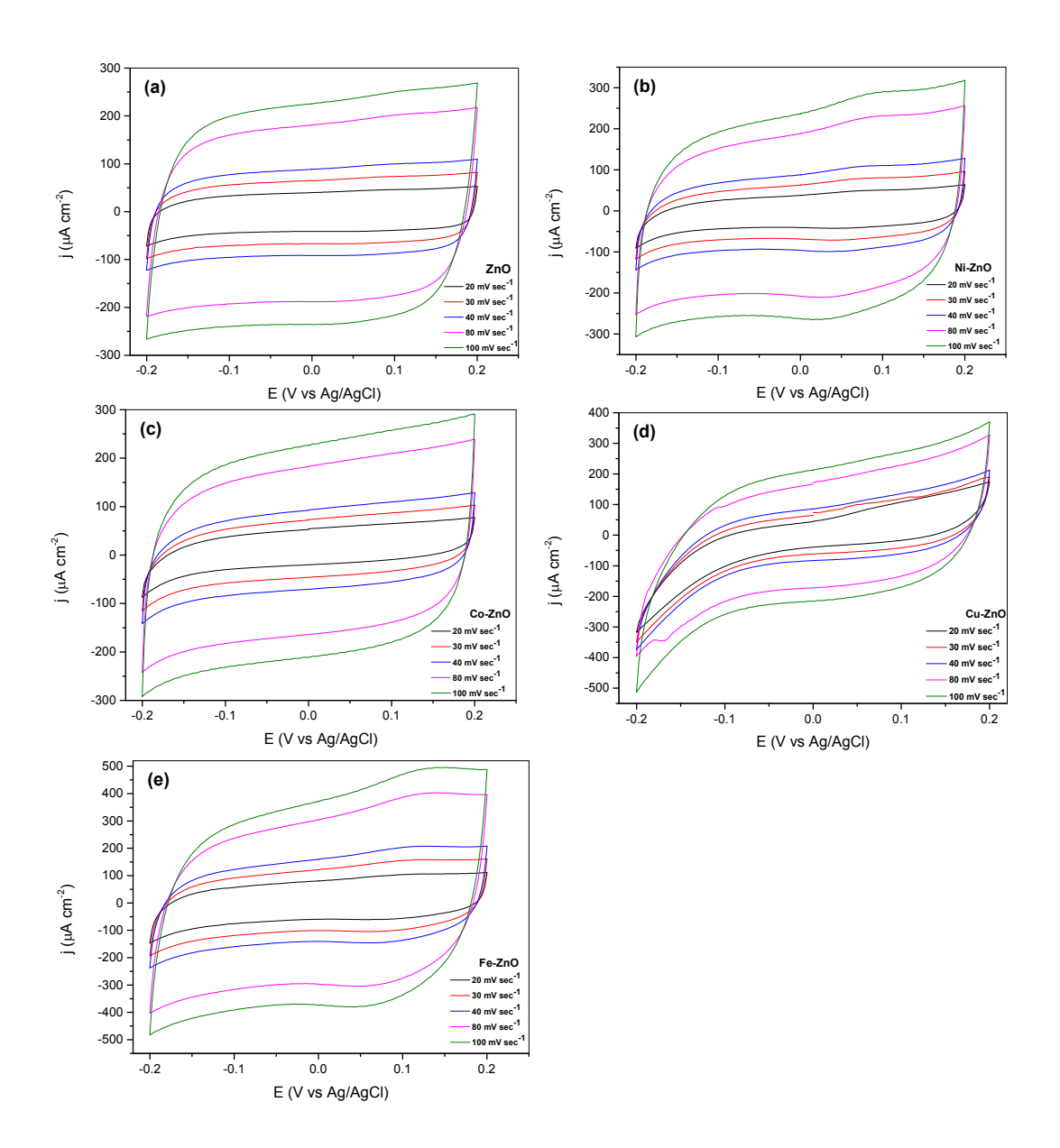


Figure S9: The Cyclic Voltammetry obtained for scan ranges of 20-100 mV sec⁻¹. Measurements were conducted in 0.1 NaClO₄(Ar saturated) in an H-Cell configuration. a.) ZnO GDE, b.) Ni-ZnO GDE, c.) Co-ZnO GDE, d.) Cu-ZnO GDE, e.) Fe-ZnO GDE.

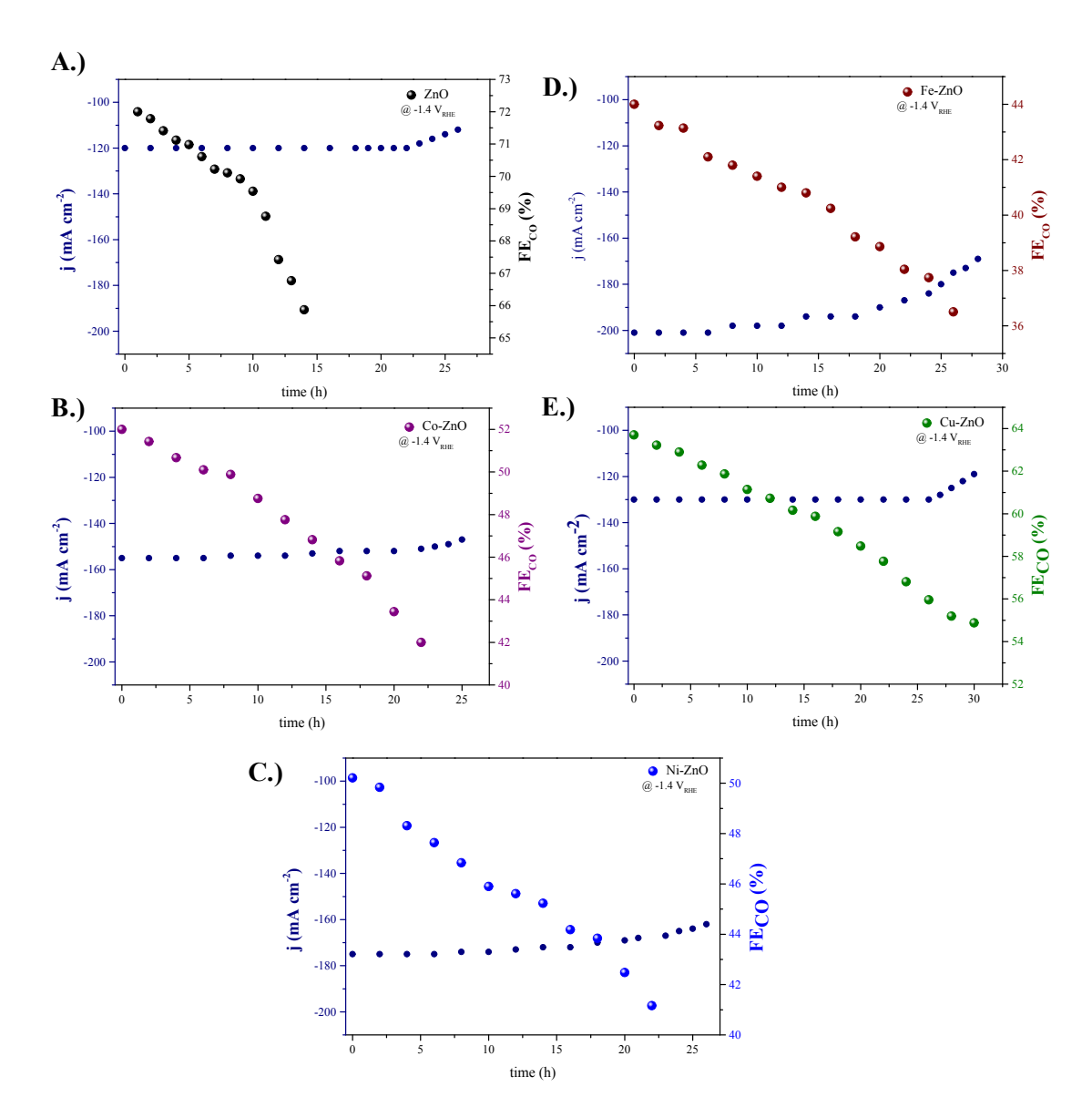


Figure S10: Response of total current density (j) and faradaic efficiency (FE_{CO}) during the stress test of constant potentiostatic conditions (-1.4 V_{RHE}). A.) Stability of the ZnO GDE, B.) Stability of the Co-ZnO GDE, C.) Stability of the Ni-ZnO GDE, D.) Stability of the Fe-ZnO GDE, E.) Stability of the Cu-ZnO GDE.

The double-layer capacitance (C_{dl}) was calculated according to the formula:

$$C_{dl} = Ja + \frac{|Jc|}{scan - rate}$$

 J_a = the recorded current density at the anodic part of the CV with a specific scan rate.

 J_c = the recorded current density at the cathodic part of the CV with a specific scan rate.

Scan-rate of a specific CV sweep [mV sec-1], C_{dl} [mF]

The Faradaic efficiency for gas products was calculated using the following formula:

$$FE (\%) = (z \cdot c \cdot v \cdot F \cdot P)/(I \cdot R \cdot T)$$

z = number of e needed for the product formation (2 e- for CO formation).

c = concentration of the product in the gas-outlet stream.

v = flow rate of the gas-outlet stream (sccm).

F = 94685 C mol-1

P = 101325 Pa

R = 8.314 J mol-1 K-1

T = 298 K

I = total current passed through the cathode

The FE was calculated based on the gas flow rate measured at the flow-cell outlet for the polarization curve's selected points. The gas product was quantified using a Tesko Agilent micro GC and a TCD detector. The liquid product analysis was done through Ionic Chromatography for the catholyte aliquots.

The rate of the relative deterioration of the FE_{CO} of the GDEs was determined according to the ratio: $\frac{\Pi FE co}{\Delta h} [h^{-1}]$

 $\Pi FEco$ = the percentage of relative decrease of the FE_{CO} .

 Δh = time frame of measurement

$$\Pi FEco = \frac{FE1 - FE2}{FE1} 100\%$$

FE2= the final FE_{CO} of the GDEs.

The Faradaic efficiency for liquid products was calculated using the following formula:

$$FE (\%) = (z \cdot c \cdot V \cdot F \cdot 100\%)/(Q)$$

z = number of e⁻ needed for the product formation (2 e- for HCOO⁻ formation).

c = concentration of the product in catholyte.

V = Volume of the catholyte.

F = 94685 C mol-1

Q = total charge passed through the cathode

The FE was calculated based on the gas flow rate measured at the flow-cell outlet for the polarization curve's selected points.

A practical approach of the available active sites and the TOF for CO (TOF_{CO}) of the catalysts was calculated using the following formulas:

$$\mu = A_s \frac{N * m}{Mcat}$$

 μ = concentration of active sites [cm⁻²].

 $A_s = \frac{\textit{Cdl, cat}}{\textit{Cdl, ZnO}}$, where C_{dl} is the double layer capacitance as calculated by the ECSA.

The A_s ratio describes the total available catalyustic centers over the materials surface, in relation with the standard ZnO catalyst.

 $N = N_A$ the Avogadro number, 6.023•10²³ [atoms moles⁻¹].

m =the loading of the catalyst material over the GDE, 0.8 mg cm⁻².

 M_{cat} = the molecular weight (MW) of the catalyst [g mol⁻¹].

For the composite materials composed of ZnO and metal-oxide (MO) phases, their molecular weight is calculated: $M_{cat} = 0.8MW(ZnO) + 0.2MW(MO)$.

$$TOF_{CO} = \frac{Jco}{n * e * u}$$

 TOF_{CO} = turn over frequency (TOF) for CO [s⁻¹].

 J_{CO} = partial current density for CO at -1.2 V (vs RHE) overpotential.

 μ = concentration of active sites [cm⁻²].

n =the number of e^{-2} required for the CO formation, $2e^{-1}$.

e = the elementary charge, $1.602 \cdot 10^{-19}$ C.

Information about the micro strain were provided through the following formula:

$$\varepsilon = \frac{\beta}{4 * tan\theta}$$

 ε = micro strain value (%) in the crystalline field of the ZnO phase.

 β = is the line broadening at FWHM in radians, Gausian fitted peak.

 θ = the Bragg's angle in degrees, half of 2 θ .

The diameter of the crystallites was calculated using the Bragg's law:

$$D = \frac{K * \lambda}{\beta * \cos \theta}$$

D = crystalline diameter (nm).

 β = is the line broadening at FWHM in radians.

 θ = the Bragg's angle in degrees, half of 2 θ .

K = diffraction order, 0.94

 λ = radiation wavelength, 1.5406 Å.

The effect of the different phases to the ε of the ZnO phase, was assessed over the ZnO-wurtzite peak of 56.8°. The diffractogramm's peak overlap of the different phases with the ZnO and the altering of the crystalline grain size (D) made the e estimation inaccurate at different 20 values.

Table S1: Values of the catalysts' micro strain for the ZnO peak of 56.8°.

Catalyst	2θ	β	D	ε (10-3)
ZnO	56.8	0.32351	29.15	2.61
Cu/ZnO	56.74	0.35082	26.88	2.83
Co/ZnO	56.64	0.46172	22.61	3.37
Ni/ZnO	56.72	0.37285	25.29	3.01
Fe/ZnO	56.84	0.87233	20.81	6.03

Table S2: Values of the catalysts' intrinsic catalytic properties.

Catalyst	MW	J_{CO}	μ	TOF _{CO}
ZnO	81.38	-101	9.83•10 ¹⁷	0.32
Cu/ZnO	81.01	-120	8.77•10 ¹⁷	0.41
Co/ZnO	113.26	-81	6.59•10 ¹⁷	0.215
Ni/ZnO	80.09	-64	11.41 •10 ¹⁷	0.176
Fe/ZnO	97.04	-60	13.51 •10 ¹⁷	0.142

Table S3: Performance comparison of different Zn-based catalysts.

Catalyst	System	Performance, FE _{CO}	Stability	Reference
nanoporous ZnO	H-cell	-1.66 V (Ag/AgCl), 92%	-	1
Zn/ZnS	H-cell	-1 V (RHE), 94%	15 h	2
Porous Zn	H-cell	-1.1 V (RHE), 80%	-	3
Hexagonal Zn	H-cell	-1.1 V (RHE), 80%	30 h	4
Zn/ZnO	H-cell	-2.4V (Ag/AgCl), 90%	5 h	5
Nanostructured Zn	H-cell	-1.1 V (RHE), 80%	12 h	6
ZnO nanosheets	H-cell	-1.1 V (RHE), 85%	8 h	7
Ag@ZnO@rGO	H-cell	-1.6 V (SCE), 70%	2 h	8
OD-Au	H-cell	-10 mA cm ⁻² , 90%	8 h	9
ZnAg	H-cell	-1 V (RHE), 84%	9 h	10
ZnO/biochar	Flow-cell	$J_{CO} = -64 \text{ mA cm}^{-2}$	14 h	11
ZnO nanoparticles	Flow-cell	$J_{CO} = -80 \text{ mA cm}^{-2}$	10 h	12
Porous-Zn	Flow-cell	$J_{CO} = -48 \text{ mA cm}^{-2}$	8 h	13
FePc	Flow-cell	$J_{CO} = -30 \text{ mA cm}^{-2}$	24 h	14
ZnO @ MO	Flow-Cell	$J_{\rm CO}$ = -80 mA cm ⁻²	30 h	This work

References

- (1) Jiang, X.; Cai, F.; Gao, D.; Dong, J.; Miao, S.; Wang, G.; Bao, X. Electrocatalytic Reduction of Carbon Dioxide over Reduced Nanoporous Zinc Oxide. *Electrochemistry Communications* **2016**, *68*, 67–70. https://doi.org/10.1016/j.elecom.2016.05.003.
- (2) Li, C.; Shen, G.; Zhang, R.; Wu, D.; Zou, C.; Ling, T.; Liu, H.; Dong, C.; Du, X.-W. Zn Nanosheets Coated with a ZnS Subnanometer Layer for Effective and Durable CO2 Reduction. *J. Mater. Chem. A* **2019**, *7* (4), 1418–1423. https://doi.org/10.1039/C8TA10799H.
- (3) Lu, Y.; Han, B.; Tian, C.; Wu, J.; Geng, D.; Wang, D. Efficient Electrocatalytic Reduction of CO2 to CO on an Electrodeposited Zn Porous Network. *Electrochemistry Communications* **2018**, *97*, 87–90. https://doi.org/10.1016/j.elecom.2018.11.002.

- (4) Won, D. H.; Shin, H.; Koh, J.; Chung, J.; Lee, H. S.; Kim, H.; Woo, S. I. Highly Efficient, Selective, and Stable CO2 Electroreduction on a Hexagonal Zn Catalyst. *Angewandte Chemie International Edition* **2016**, *55* (32), 9297–9300. https://doi.org/10.1002/anie.201602888.
- (5) Xiang, Q.; Li, F.; Wang, J.; Chen, W.; Miao, Q.; Zhang, Q.; Tao, P.; Song, C.; Shang, W.; Zhu, H.; Deng, T.; Wu, J. Heterostructure of ZnO Nanosheets/Zn with a Highly Enhanced Edge Surface for Efficient CO2 Electrochemical Reduction to CO. *ACS Appl. Mater. Interfaces* **2021**, *13* (9), 10837–10844. https://doi.org/10.1021/acsami.0c20302.
- (6) Li, P.; Liu, J.; Bi, J.; Zhu, Q.; Wu, T.; Ma, J.; Zhang, F.; Jia, J.; Han, B. Tuning the Efficiency and Product Composition for Electrocatalytic CO2 Reduction to Syngas over Zinc Films by Morphology and Wettability. *Green Chem.* **2022**. https://doi.org/10.1039/D1GC04364A.
- (7) Geng, Z.; Kong, X.; Chen, W.; Su, H.; Liu, Y.; Cai, F.; Wang, G.; Zeng, J. Oxygen Vacancies in ZnO Nanosheets Enhance CO2 Electrochemical Reduction to CO. *Angewandte Chemie International Edition* **2018**, *57* (21), 6054–6059. https://doi.org/10.1002/anie.201711255.
- (8) Nguyen, V.-H.; Thi Vo, T.-T.; Huu Do, H.; Thuan Le, V.; Nguyen, T. D.; Ky Vo, T.; Nguyen, B.-S.; Nguyen, T. T.; Phung, T. K.; Tran, V. A. Ag@ZnO Porous Nanoparticle Wrapped by RGO for the Effective CO2 Electrochemical Reduction. *Chemical Engineering Science* **2021**, *232*, 116381. https://doi.org/10.1016/j.ces.2020.116381.
- (9) Chen, Y.; Li, C. W.; Kanan, M. W. Aqueous CO2 Reduction at Very Low Overpotential on Oxide-Derived Au Nanoparticles. *J. Am. Chem. Soc.* **2012**, *134* (49), 19969–19972. https://doi.org/10.1021/ja309317u.
- (10) Guo, W.; Shim, K.; Kim, Y.-T. Ag Layer Deposited on Zn by Physical Vapor Deposition with Enhanced CO Selectivity for Electrochemical CO2 Reduction. *Applied Surface Science* **2020**, *526*, 146651. https://doi.org/10.1016/j.apsusc.2020.146651.
- (11) Lourenço, M. A. O.; Zeng, J.; Jagdale, P.; Castellino, M.; Sacco, A.; Farkhondehfal, M. A.; Pirri, C. F. Biochar/Zinc Oxide Composites as Effective Catalysts for Electrochemical CO2 Reduction. *ACS Sustainable Chem. Eng.* **2021**, *9* (15), 5445–5453. https://doi.org/10.1021/acssuschemeng.1c00837.
- (12) Zeng, J.; Fontana, M.; Sacco, A.; Sassone, D.; Pirri, C. F. A Study of the Effect of Electrode Composition on the Electrochemical Reduction of CO2. *Catalysis Today* **2021**. https://doi.org/10.1016/j.cattod.2021.07.014.
- (13) Wang, J.; Zhu, Z.; Wei, X.; Li, Z.; Chen, J. S.; Wu, R.; Wei, Z. Hydrogen-Mediated Synthesis of 3D Hierarchical Porous Zinc Catalyst for CO2 Electroreduction with High Current Density. *J. Phys. Chem. C* **2021**. https://doi.org/10.1021/acs.jpcc.1c07498.
- (14) Torbensen, K.; Han, C.; Boudy, B.; von Wolff, N.; Bertail, C.; Braun, W.; Robert, M. Iron Porphyrin Allows Fast and Selective Electrocatalytic Conversion of CO2 to CO in a Flow Cell. *Chemistry A European Journal* **2020**, *26* (14), 3034–3038. https://doi.org/10.1002/chem.202000160.